Research Square

Preprints are preliminary reports that have not undergone peer review.
They should not be considered conclusive, used to inform clinical practice,
or referenced by the media as validated information.

Amniotic Fluid Stem Cell-Derived Secretome MRG1061 Improves Alveolarisation and Reduces Lung Inflammation in Experimental Bronchopulmonary Dysplasia

Fabian Doktor
Hospital for Sick Children
Andrew Parnell
Micregen Ltd.
Lina Antounians
Hospital for Sick Children
Daniel Feist
Micregen Ltd.
Ben Mellows
Micregen Ltd.
Rebeca Lopes Figueira
Hospital for Sick Children
Victoria Fortuna
Hospital for Sick Children
Kasra Khalaj
Hospital for Sick Children
Atiyeh Asadpour
University of Reading
Emily Lo
Hospital for Sick Children
Anand Rai
Micregen Ltd.
Steve Ray
Micregen Ltd.
Kaya Stasiewicz
Hospital for Sick Children
Darius Widera
University of Reading
Augusto Zani
Hospital for Sick Children

Ketan Patel
Micregen Ltd.
Robert Mitchell
robertmitchell@micregen.com

Micregen Ltd.

Research Article

Keywords: Neonatal, lung injury, stem cells, regenerative medicine, secretome, inflammation

Posted Date: October 27th, 2026

DOI: https://doi.org/10.21203/rs.3.rs-10150924/v1

License: This work is licensed under a Creative Commons Attribution 4.0 International License.
Read Full License

Additional Declarations: Competing interest reported. RM, AP, KP, SR are employed by Micregen Ltd.

Abstract

Background

Mesenchymal stromal cell (MSC)-derived secretomes are emerging as scalable, cell-free candidates for regenerative and immunomodulatory therapy, but their mechanistic cargo signatures and translational potential remain incompletely defined. We developed MRG1061, a clinically translatable, amniotic fluid-derived stem cell (AFSC)-derived secretome produced using the proprietary Secretomix® platform, and sought to define its protein cargo, predict key inflammatory and regenerative pathways, and functionally validate these predictions in human *in vitro* systems and an *in vivo* model of lung injury.

Methods

Proteomic profiling of MRG1061 was performed across multiple batches and analysed using pathway enrichment and disease-annotation tools to identify inflammation- and repair-relevant signatures, including blinded enrichment for bronchopulmonary dysplasia (BPD) and related chronic inflammatory conditions. Predicted anti-inflammatory and regenerative activities were then tested in human *in vitro* assays using lipopolysaccharide-stimulated peripheral blood mononuclear cells, an NF-κB reporter lung adenocarcinoma cell line, primary human alveolar epithelial cells, and human lung fibroblasts. To assess *in vivo* relevance, MRG1061 was evaluated in a neonatal hyperoxia-induced lung injury model, with quantitative analyses of lung structure and inflammatory gene expression. A separate study in healthy mice assessed systemic safety by repeated dosing and serum biochemistry.

Results

MRG1061 contained extracellular vesicles and a complex protein cargo enriched for pathways linked to innate and adaptive immune regulation, NF-κB signalling, redox homeostasis, apoptosis, and disease annotations that included BPD. Consistent with these predictions, MRG1061 reduced inflammatory gene and protein expression and NF-κB activity in human immune and lung epithelial assays, modulated disturbed proliferation of primary human alveolar epithelial cells, and decreased stress-induced senescence in lung fibroblasts. In neonatal hyperoxia-exposed mice, MRG1061 improved lung architecture and attenuated expression of key inflammatory cytokines and inflammasome components. Repeated administration to healthy mice revealed no adverse effects on survival or standard serum biochemical parameters.

Conclusions

MRG1061 exhibits a cargo-defined, multi-modal anti-inflammatory and regenerative profile that translates into measurable effects in human *in vitro* systems and *in vivo* lung injury, while maintaining a

favourable safety signal in healthy animals. These data support further development of MRG1061 as a stem cell-free biologic for inflammatory and degenerative lung disease.

Background

Preterm birth, characterised as birth before 37 weeks of gestation, is increasing in prevalence, affecting up to 14% of live births globally (1). While the survival rates of preterm neonates are improving, short- and long-term morbidity continues to be a significant challenge. Preterm birth is associated with lung injury and increased susceptibility to developing chronic lung disease, including bronchopulmonary dysplasia (BPD) (2). Thus the prevalence of BPD is increasing as a result of increased survival of extremely low gestational age newborns (ELGAN) (1).

Normal lung development starts *in utero* from an early embryonic stage around the 4th week of gestation, completing branching morphogenesis midway through gestation (16–26 weeks) in the foetal canalicular stage. The remaining gestational time is devoted to the expansion of airspaces during the saccular stage, mesenchymal to epithelial transition, and the formation of capillaries and vessels. Lung development continues postnatally through the alveolar stage throughout childhood with the formation of a dense alveolar-capillary network. When born prematurely, at the threshold of viability around the 22nd week of gestation, the lung epithelial, mesenchymal, and endothelial niche is not fully established, with fewer alveolar type 1 (AT1) and type 2 (AT2) cells, the latter responsible for surfactant production (3–5). This developmental immaturity predisposes the preterm lung to injury from the supportive interventions required for survival, leading to chronic lung inflammation, microvascular impairment, and arrested lung alveolarisation (1, 2, 6). Despite advances in neonatal care, including improved ventilation strategies and surfactant replacement, BPD remains a major cause of mortality and long-term morbidity in this vulnerable population.

Although administration of caffeine, topical surfactant, steroids, and less invasive ventilation strategies have improved mortality associated with BPD, its prevalence and inherent sequalae have barely changed in the last two decades (2, 7–14). Therefore, novel innovative therapeutic options that can address the multifactorial nature of BPD are urgently needed to treat and prevent the development and progression of chronic lung disease in preterm neonates. Given that BPD involves multiple disrupted cellular and molecular pathways, therapies capable of broadly modulating inflammation, angiogenesis, and repair, such as stem cell-based approaches, offer particular promise. As such, multipotent mesenchymal stromal cells (MSCs) and their derivatives have been tested in experimental BPD models with promising preclinical results. Translation of this therapy with whole cells has been initiated with ongoing phase 1/2 trials in BPD patients (2, 15). Studies introducing MSCs have shown weak engraftment into their target tissue, suggesting a paracrine mechanism of action (16–18). Indeed, multiple studies have used the paracrine factors from the cells (“secretome”) or specific fractions, such as MSC extracellular vesicles (EVs), to treat experimental BPD in small and large animal models with promising results, specifically via the exertion of immunomodulatory properties (19–22).

Among the various stem cell sources, amniotic fluid-derived stem cells (AFSCs) are particularly attractive due to their accessibility, multipotency, and favourable ethical and safety profiles (23, 24). Their pulmonary regenerative and anti-inflammatory potential has been explored in various experimental models, including rodent models of congenital diaphragmatic hernia (CDH) or bleomycin-induced lung fibrosis (17, 25). Similar to other stem cell sources, their regenerative capabilities rely on paracrine signalling, which has been demonstrated using EVs derived from AFSCs in the treatment of experimental foetal pulmonary hypoplasia (26–33). Building on this evidence, we developed MRG1061, a proprietary, clinically and GMP translatable amniotic fluid-derived stem cell secretome generated using the Secretomix® platform. In this study, we aimed to characterise the composition of MRG1061 and evaluate its potential to modulate key pathways involved in BPD. To this end, we combined proteomic and bioinformatic analysis of the MRG1061 cargo with functional assays in human immune and lung cells, tested its efficacy in a neonatal hyperoxia model of experimental BPD and performed an initial *in vivo* safety assessment to support future clinical translation.

Methods

Flow cytometry

AFSC were non-specifically blocked with 2% FBS. Antibodies (multipotency markers: CD73 (Miltenyi Biotech, 130-112-062), CD90 (Miltenyi Biotech, 130-114-864), CD105 (Miltenyi Biotech, 130-112-324) and non-MSC markers: CD34 (Miltenyi Biotech, 130-120-515), CD45 (Miltenyi Biotech, 130-110-631), CD14 (Miltenyi Biotech, 130-110-518), CD19 (Miltenyi Biotech, 130-114-171), HLA-DR (Miltenyi Biotech, 130-111-942) were incubated on the cells for 1h at 4°C. Ten thousand events were profiled by flow cytometry (Intellicyt iQue screener) followed by data analysis with ForeCyt software.

Multipotency assessment

For assessment of adipogenic and osteogenic potential, 4,000 cells/cm^2 were plated and cultured to 95% confluency before growth media were replaced with either adipogenic (R&D Systems CCM007 and CCM011) or osteogenic (Life Technologies A10069-01 and A10066-01) differentiation media for 21 days. Adipogenesis or osteogenesis was determined by Oil Red O (Sigma Aldrich O0625) or Alizarin Red S (Sigma Aldrich A5533) staining respectively. Brightfield images were captured immediately after staining. Chondrogenic potential was assessed by resuspending 1 × 10^6 cells in a 1.5 mL tube and allowing the formation of a pellet by gravity. The pelleted cells were incubated in differentiation media (Life Technologies A10069-01 and A10064-01) for 21 days with a media change every 3 days. Chondrogenic cells were identified with 0.1 mg/mL Alcian Blue staining solution (Sigma Aldrich A5268).

TEM

Preparations were mixed with equal volumes of 4% paraformaldehyde in EM-grade PBS. 25 µL of each preparation was deposited onto charged Formvar-carbon-coated grids. Each preparation was repeated in duplicate grids. Samples were incubated for 1 h at room temperature, followed by PBS washes, fixation in 1% glutaraldehyde for 10 min, distilled water washes, contrasting in uranyl oxalate for 10 min, and embedding with methyl cellulose-uranyl acetate for 10 min. Grids were then placed into a Tecnai 20 transmission electron microscope (FEI, Hillsboro, OR) and imaged from 25,000X to 100,000X magnification.

NTA analysis

Samples were diluted in PBS and introduced into the LM10 system (NanoSight Ltd, Salisbury, UK). The LM10 system was calibrated using 100 nm polystyrene beads and five 30-second videos were collected, averaged, and analysed using a 65 mWatt 405 nm violet laser. At capture with sCMOS camera on NTA 3.1, with Build 3.1.46 software, the temperature was 22°C. The Brownian motion of EVs moving across the field was tracked by the software to calculate size. The size distribution of EVs and the concentration of particles per mL in the sample were then determined, providing information about the population of EVs and their size range.

Western blot characterisation

Western blot characterisation
Proteins were extracted from MRG1061 and quantified using Pierce Bradford assay. 40 µL of each preparation was reduced with 4X reducing agent and 10X sample buffer and loaded onto SDS PAGE gels. Protein was then transferred to polyvinylidene difluoride membranes, which were pre-blocked in EveryBlot Blocking Buffer (Bio-Rad), washed in TBST, and incubated with primary and secondary antibodies listed in **Table 4**. Blots were visualized using enhanced chemo-luminescence.

Sample preparation for mass spectrometry (MS) and analysis

Samples were processed as previously described (34, 35). Briefly, proteins from three MRG1061 secretome batches were separately denatured, reduced and alkylated before being digested via trypsinisation. Elution's were combined and acidified with trifluoroacetic acid to a final concentration of 1% before finally being purified/desalted. LC-MS/MS measurements were performed on a QExactive Plus mass spectrometer (Thermo Scientific) coupled to an EasyLC1000 nanoflow-HPLC, and samples were applied directly onto an organic gradient column without a pre-column at a flow rate of 250 nL/min and for sample application 600 nL/min. The mass spectrometer was operated in the data-dependent mode and switched automatically between MS (max. of $1x10^6$ ions) and MS/MS followed by a maximum of ten MS/MS scans using normalised collision energy of 25% and a target value of 1000. The mass range for MS was m/z = 370–1750. The resolution for MS was set to 70,000 and for MS/MS to 17,500. The MS

raw data files were uploaded into the MaxQuant software version 1.6.2.10 for peak detection, generation of peak lists of mass error corrected peptides, and for database searches.

Bioinformatics

Gene set over-representation analysis was performed using PANGEA (Pathway, Network and Gene-set Enrichment Analysis), version 2 (beta; https://www.flyrnai.org/tools/pangea/web/home/9606, accessed May 2026), a multi-species enrichment tool developed by the *Drosophila* RNAi Screening Center (DRSC) at Harvard Medical School. Two gene lists derived from the MRG1061 proteomic dataset were analysed independently: the complete list of proteins surviving positive Pareto scaling (n – 1,136 of 1,907 qualified features) and a focused subset comprising the 20 most abundant proteins by iBAQ ranking. Only proteins present in all three samples were included in further analysis. Gene symbols were entered as Human gene names and enrichment was tested against the complete human genome background (taxonomy ID: 9606) using a hypergeometric test, executed via the PypeR function in R, to identify gene sets significantly over-represented relative to random expectation. Five gene-set resources were queried: Direct GO Biological Processes (category ID: 83), Direct GO Cellular Component (category ID: 84), Direct GO Molecular Function (category ID: 85), REACTOME Pathway (category ID: 143), and Disease annotation AGR. Direct GO term annotation was selected to avoid redundancy associated with hierarchical GO term propagation, ensuring that each protein was assigned only to the most specific GO term for which direct experimental evidence exists.

Results were initially filtered by raw p-value (< 0.1). Adjusted p-values were calculated using Bonferroni correction, the Benjamini-Hochberg false discovery rate (FDR), and the Benjamini-Yekutieli procedure, and are reported alongside raw p-values for every enriched term in supplementary (**Supplementary Table S1**).

Inflammation-relevant enrichments shown in Fig. 2 and Tables 1–2 were identified by applying a pre-specified, tiered, regex-based keyword library to the enriched gene-set names. The library comprises a Tier A set covering canonical inflammation and immune biology (inflammation, immune, cytokine, chemokine, interleukin, interferon, NF-κB, TNFα, complement, MHC / HLA, antigen processing, phagocytosis, neutrophil/macrophage/lymphocyte/T-cell/B-cell biology, JAK/STAT, Toll-like receptors, defensins, antimicrobial, chemotaxis, sepsis, LPS, caspase, NLR/NOD, immunoglobulin, prostaglandin/leukotriene, autoimmunity), and a Tier B set covering inflammation-adjacent processes relevant to BPD pathophysiology (oxidative stress / redox, glutathione, peroxidase, superoxide, catalase, apoptosis / programmed cell death, fibrosis / fibroblast / myofibroblast, extracellular matrix, collagen, angiogenesis, endothelial biology, hypoxia, wound healing, tissue repair, epithelial-mesenchymal transition, alveolar / lung development / surfactant biology, TGF / VEGF / MAPK / ERK / p38 signalling). For the Disease annotation AGR category, the keyword set was augmented with respiratory disease names relevant to BPD (bronchopulmonary, pulmonary, respiratory, asthma, pneumonia, chronic obstructive, COPD, emphysema) and chronic inflammatory conditions (IBD, colitis, Crohn's disease,

arthritis, rheumatic, psoriasis, granulomatous). Keyword matching was case-insensitive and substring-based; tier and matched keyword are reported alongside each curated term in **Supplementary Table S2**.

Enrichment results were visualised as: an analysis-workflow schematic (Fig. 2A); a dot plot of the top inflammation-relevant REACTOME pathways from the full protein list (Fig. 2B, dot size proportional to overlap count following GSEA convention, colour scaled to -log10 BH-FDR); category-stratified horizontal bars summarising the top inflammation-relevant Direct GO Biological Process, Cellular Component and Molecular Function terms from the full protein list (Fig. 2C); a forest plot of inflammation-relevant Disease annotation AGR enrichments, anchored on bronchopulmonary dysplasia (Fig. 2D); and a bipartite protein-pathway network linking the 20 most abundant cargo proteins to the inflammation-relevant pathways they participate in (Fig. 2E). Vector figures were generated in Python (matplotlib v3.10) with network layouts computed in NetworkX v3.4.

RNA extraction and gene expression quantification

For *in vitro* assessment of inflammatory genes, RNA was isolated from human PBMCs using an RNeasy kit (Qiagen 74104). Briefly, approximately 2 million PBMCs were lysed in Buffer RLT before collection and cDNA synthesis using RevertAid RT Kit and 5,000 ng RNA. 4 µL of cDNA was utilised for each biological replicate, together with 11 µL of a master mix comprising 7.5 µL SYBR™ Green Master Mix and 0.15 µL of both forward and reverse primers. We analysed the expression of several inflammatory markers including human tumour necrosis factor alpha (hTNFα), human Nuclear factor kappa-light-chain-enhancer of activated B cells (hNF-κB), interleukin 10 (hIL10), interleukin 1β (hIL1β), interleukin 6 (hIL6) and caspase 1 (hCasp1). As a reference gene, glyceraldehyde-3-phosphate dehydrogenase (hGAPDH) was used.

To extract RNA from *in vivo* studies, lung tissue was exposed to Trizol and cDNA synthesis using 1,000 ng RNA was conducted using the VILO cDNA synthesis kit, as previously described (36). cDNA was kept at -20°C until RT-qPCR was conducted, which was performed in accordance with the MIQE guidelines (37). In summary, 5.5 µL of cDNA was utilised for each biological replicate, along with 6 µL of a master mix comprising 5.5 µL SYBR™ Green Master Mix and 0.25 µL of both forward and reverse primers. The primer sequences were designed using Primer3 software based on mouse sequences available in the National Center for Biotechnology Information Nucleotide database and are detailed in Table 1. Gene expression was calculated using the $2^{\Delta\Delta}$Ct. The expression of multiple markers including tumour necrosis factor alpha (mTNFα), monocyte chemoattractant protein-1 (mMCP1), caspase 1 (mCasp1), interleukin 18 (mIL18) and FGF10 (rFGF10) were analysed. As a reference gene, succinate dehydrogenase complex subunit A (mSdha) was used.

NF-κB luciferase gene reporter assays

A549 cells (Cell line Service, Eppelheim, Germany) transduced with a lentiviral pGreenFireTM-NF-κB-GFP-Luciferase Reporter construct (System Biosciences) (38) were cultivated in Ham's F-12 (Sigma-Aldrich)

containing 1% L-glutamine (200 mM, Sigma-Aldrich) and 10% FBS (Sigma-Aldrich) at 37°C, 5% CO_2. A549 NF-κB reporter cells (1 x 10^4 cells/well) were plated in 96-well plates and incubated for 24 hours to allow attachment. Following this, cells were pretreated for 24 h with 2% MRG1061 and then serum-starved for 4 h in medium containing 0.01% BSA at 37°C in a 5% CO_2 incubator with 2% (v/v) MRG1061 added to the appropriate wells. Subsequently, the cells were returned to complete medium supplemented with serum and treated with 2% MRG1061 and TNFα (10 ng/mL) for 24 hours. After incubation, the culture medium was replaced with DMEM without phenol red (Sigma-Aldrich, UK), and Bright-Glo® substrate (Promega, UK) was added directly to the wells according to the manufacturer's protocol. Luminescence was measured using a SpectraMax i3x microplate reader (Molecular Devices, UK). This setup quantifies NF-κB activity based on the luminescence intensity generated by reporter gene expression.

TNFα concentration (ELISA)

Whole human blood was collected using a heparin-coated vacutainer® before being diluted 1:1 in RPMI media (Gibco 11875093) and PBMCs isolated via centrifugation with Lymphoprep (Stemcell Technologies 07851) (1,200 rcf, 10 min at room temperature with brake). The supernatant was transferred to a sterile container and diluted to 4x original blood volume with RPMI media.

800 µL isolated PBMC/RPMI was added to a 24 well plate together with 100 µL MRG1061 before being incubated for 1 h. Following incubation, 100 µL of 10 ng/mL E. coli LPS/RPMI media was added to each 'stressed' well with only RPMI media to control wells and the cells incubated for a further 5 h at 37ºC, 5% CO_2. Following incubation, the suspension was centrifuged at 2,000 rcf for 20 min and the supernatant collected and frozen at -80ºC.

TNFα concentration was measured via ELISA (R&D Systems DY210) following manufacturers instructions. Briefly, a 96 well plate was coated overnight at room temperature with 100 µL of the Capture Antibody before 1 h blocking and addition of test sample or standards for a 2 h incubation at room temperature. 100 µL Detection Antibody was added for a 2 h incubation before protein concentration was detected at 450 nm absorbance following incubation for 20 min with Streptavidin-HRP.

Cell culture and EdU staining

Primary human pulmonary alveolar epithelial airway cells were cultured under normoxic conditions until they reached 70% confluency. Cells were nourished with alveolar epithelial cell medium (AEpiCM). After reaching confluency, cells were either left untreated (control group), or treated with a 2.5 µmol NSC23766, an inhibitor of RAC1 (Rho GTPase) alone or incubated together with MRG1061 (1:10 total medium volume). After 24 h, cells were fixed with 4% PFA and an EdU staining was performed with nuclear Hoechst counterstaining according to the manufacturer's suggested protocol. Cells were then imaged with a 3D HISTECH slide scanner and positive cells were counted as a ratio to Hoechst+ cells. Representative images at a higher resolution were taken via Leica SP8 lightning confocal microscopy. Total number of Hoechst+ cells was estimated using ImageJ.

Senescence

Lung fibroblast IMR90 cells were seeded at 10,000 cells/cm^2 and allowed to adhere. Once adhered, 50 μM etoposide was added to fresh culture media and incubated on the cells for 48 h at 37°C, 5% CO_2. Following incubation, saline or MRG1061 was added to the plate at a concentration of 25% v/v in culture media and incubated for another 48 h before the cells were fixed and processed with Senescence Detection Kit (Abcam ab65351) as per manufacturers instructions. Briefly, Staining Solution Mix was added at 1 mL/well and incubated for 18 h in the dark at 37°C in atmospheric conditions. Following 18 h incubation, the cells were washed and imaged using bright-field microscopy at 10X magnification. Senescent cells were indicated by the blue staining of β-galactosidase.

Ethical and supporting

Ethical approval

was sought for the animal studies conducted at The Hospital for Sick Children, Toronto, Canada from the Animal Care Committee (AUP #1000065164) and conducted under the Project title: Stem cell therapy in a mouse model of bronchopulmonary dysplasia.

Animal research was conducted in the United Kingdom in accordance with 'ANIMALS (SCIENTIFIC PROCEDURES) ACT 1986' under a UK Home Office license (ref: PP8799872, Project title: Microvesicles and the prevention of tissue wasting) at the University of Reading (establishment license: XF75DBBCB). Work under this license was reviewed and approved by the University of Reading's Animal Welfare and Ethics Review Board. Animals were received from a licensed UK breeder and maintained under standard husbandry conditions (controlled environment with *ad libitum* food and water). All study reporting was aligned with ARRIVE 2.0 guidelines.

For the BPD *in vivo* study, sample size per group was determined a priori based on the average litter size of C57Bl/6 dams (8 mice per litter), providing double the numbers of controls due to rotation of control dams from hyperoxia to normoxia to prevent oxygen toxicity. Inclusion/exclusion criteria determined a priori that all surviving pups would be included into the study, with pups failing to survive the 10-day experimental set up excluded from analysis.

For the safety toxicology study, the sample size per group was determined a priori using a power calculation based on alanine aminotransferase (ALT) as the primary safety endpoint in healthy Crl:CD1 mice, assuming a 30% increase in mean ALT between treated and PBS control groups as the minimal toxicologically relevant difference, using sex-specific baseline ALT variability (for males and females at the relevant time points) as measured in preliminary controls, with an alpha level of 0.05 and 80% statistical power to ensure robust detection of clinically meaningful liver effects while minimising animal use in accordance with the 3Rs. Inclusion and exclusion criteria were established a priori, only healthy adult mice were enrolled, with exclusion prior to study initiation for any signs of ill health, and exclusion during the study or analysis limited to cases of misadministration of the test substance.

Experimental mouse model of BPD

Time mated pregnant C57BL/6J mice were placed in a hyperoxia (70%) Plexiglas chamber to induce experimental BPD or in a normoxia (21%) chamber 1 day prior to expected birth of their litter, as previously described (39). Dams were randomly assigned to the groups, but with no formal randomization software used. To minimise potential confounders, all animals were housed in the same room to expose all animals to the noise of the hyperoxia chambers, same day, night rhythm and facility staff. The day of birth was considered postnatal (P) day 0. Litter size was adjusted to 6–8 neonatal pups (40), and they were randomly assigned to either 1st) control group (n = 19), 2nd) hyperoxia group + saline alone (n = 8), or 3rd) hyperoxia + MRG1061 group (n = 5, total mice n = 4 dams, n = 32 pups). Dams were switched between hyperoxic and normoxic chambers every 24h to 48h to prevent maternal oxygen toxicity.

At P4, P6, and P8, the control and hyperoxia groups received an intraperitoneal injection (IP) of either saline or MRG1061. At P10, mice were culled via inhalation with isoflurane (4% for induction, 2–2.5% for maintenance before being increased to 5% to deeply anesthetize the animals before they were decapitated), and their lungs were harvested. In an alternating fashion, either the right or the left lobe was isolated, and the main bronchus was tied off via Silk 4 – 0 for RNA and protein extraction, before the contralateral lung lobe was inflation fixed with 4% paraformaldehyde (PFA) under 20 cm H_2O via the contralateral main bronchus. All dams and pups survived the 10-day experimental set up procedure and were included into the study.

Histological analysis of lung architecture

Lungs were embedded in OCT and sectioned at a thickness of 12 µm. The samples were stained with haematoxylin and eosin (H&E). Subsequently, H&E-stained lung sections were scanned using 3D Histech slide scanner (3DHistech Ltd., Hungary). The radial alveolar count (RAC) was measured at 10X by two blinded investigators unaware of the experimental groups, as previously described (36).

Localisation of MRG1061-EV

For *in vitro* tracking of MRG1061-EVs, A549 cells were seeded into 4 well Cell Chamber slides at 20,000 cells per chamber and incubated overnight to adhere. Cells were stained with 10 µM CellTracker Red (Invitrogen C34552) for 30 minutes at 37°C, washed 3x with PBS before 400 µg protein equivalent of EV labelled with PKH-67 (Sigma MIDI67) as per the manufacturer's instructions were incubated with the cells for 3 hours in serum-free media. Cells were fixed with 5% aqueous formaldehyde for 15 minutes and imaged with a Nikon A1R confocal microscope at 20X magnification.

In vivo safety analysis

To assess early indications of toxicity of MRG1061, 100 µL MRG1061 or sterile PBS was administered via IV bolus injection to healthy 12 week old male Crl:CD1 mice (n = 10, day 1 & 7, n = 15, day 28) and 12 week old female Crl:CD1 mice (n = 15, day 28, total mice n = 100) purchased from Charles River UK and

housed under standard husbandry in groups of 5. In accordance with ARRIVE 2.0 guidance on randomization, allocation was performed at the cage level: cages of mice were randomly assigned to control or test groups, rather than randomising individual animals within cages. Potential confounders (e.g. cage location and order of dosing) was not deliberated controlled, apart from administering injections at comparable times of day across groups. Injections were administered twice weekly, with mice culled via CO_2 inhalation and cervical dislocation at Day 1, 7 or 28. Blood was collected immediately following sacrifice via cardiac puncture into sodium citrate before plasma isolated via centrifugation (2,000 rcf) and immediately frozen until analysis using a panel of 18 biochemical markers using Beckman Coulter AU680 Analyser. A single female MRG1061 treated mouse was excluded from the study due to failure of an IV administration at the correct timepoint. Study was unblinded to researchers apart from the analysis of plasma samples.

Statistics

Analysis was performed using GraphPad Prism (version 8.2.1). Survival was calculated using the log-rank (Mantel-Cox) test. Parametric data from two experimental groups was compared using unpaired t testing (Welch correction) and non-parametric data using Mann-Whitney testing. For 3 or more experimental groups, either one way ANOVA (post-hoc Tukey's test) and Kruskal-Wallis testing (post-hoc Dunn's test) was performed if one independent variable was present, whereas two-way ANOVA was performed for more than one independent variable (post-hoc Tukey's test). For the dose-response testing (TNFα concentration), multiple comparison testing was compared to the unstimulated control. A p-value under 0.05 was considered statistically significant.

Results

Characterisation of AFSCs and identification of secreted EVs within MRG1061

We first characterised the population of GMP amniotic fluid-derived multipotent stromal cells (AFSC) as a mesenchymal stem cell (MSC) population in accordance with The International Society for Cellular Therapy (ISCT) guidelines expressing CD73, CD90 and CD105 while being negative for CD14, CD19, CD34, CD45 and HLA-DR (41). Moreover, this stem cell population also differentiated into three mesodermal lineages (adipose, cartilage and bone, Fig. 1A). By using nanoparticle tracking analysis (NTA), transmission electron microscopy (TEM), and Western Blotting, we identified and characterised an EV fraction within the secreted product MRG1061. EVs had a typical spherical or cup-shaped morphology, a mean size of 142.5 ± 2.1 nm, and showed expression of canonical EV markers such as CD63 and Tumor Susceptibility Gene 101 (TSG101) in the absence of Calnexin (CANX, Fig. 1B).

Pathway Enrichment Analysis of MRG1061 highlights its multipotent regenerative and anti-inflammatory

capabilities

To understand the molecular basis of the potential beneficial effects of MRG1061, we profiled the protein cargo through sequencing followed by bioinformatic pathway enrichment analysis using a multi-species GSEA platform, PANGEA v2 (Fig. 2A). The MRG1061 cargo proteome was significantly enriched for canonical inflammation and immune biology markers. From the full protein list, 712 enriched REACTOME pathways and 1,022 GO Biological Process terms were identified at $p < 0.1$, including: Immune system, Innate Immune System, Neutrophil degranulation, Apoptosis and Programmed Cell Death all reaching PANGEA's minimum p value (BH-FDR) of approximately 3×10^{-24}, alongside multiple NF-κB-related pathways including Dectin-1 non-canonical, NIK to non-canonical, B-Cell activation and FCERI-mediated NF-κB activation, BH-FDR $< 10^{-19}$, and the ER-Phagosome pathway (Fig. 2B and Table 1).

Table 1
Top REACTOME pathways enriched in the MRG1061 proteomic cargo (full protein list, n = 1,136).

Pathway	Gene-set ID	Set size	Overlap n	FE	P value (BH-FDR)
Immune System	R-HSA-168256	1925	238	2.21	< 1e-25 (3.4e-24)
Innate Immune System	R-HSA-168249	921	152	2.85	< 1e-25 (3.4e-24)
Neutrophil degranulation	R-HSA-6798695	430	102	4.10	< 1e-25 (3.4e-24)
Apoptosis	R-HSA-109581	165	39	8.64	< 1e-25 (3.4e-24)
Programmed Cell Death	R-HSA-5357801	186	43	7.66	< 1e-25 (3.4e-24)
Regulation of Apoptosis	R-HSA-169911	54	26	14.05	< 1e-25 (3.4e-24)
Dectin-1 mediated noncanonical NFκB signalling	R-HSA-5607761	47	27	12.28	1.8e-25 (6.0e-24)
NIK→noncanonical NFκB signalling	R-HSA-5676590	47	27	12.28	1.8e-25 (6.0e-24)
Activation of NFκB in B cells	R-HSA-1169091	51	25	10.54	3.7e-21 (7.1e-20)
FCERI mediated NFκB activation	R-HSA-2871837	65	27	8.98	3.3e-20 (5.8e-19)
ER-Phagosome pathway	R-HSA-1236974	89	32	7.68	4.9e-21 (9.3e-20)
Cellular response to hypoxia	R-HSA-1234174	65	27	8.98	3.3e-20 (5.8e-19)
MAPK6/MAPK4 signalling	R-HSA-5687128	80	29	8.09	5.8e-20 (9.9e-19)
Oxygen-dependent proline hydroxylation of HIF α	R-HSA-1234176	55	27	10.61	7.5e-23 (1.8e-21)
Defective CFTR causes cystic fibrosis	R-HSA-5678420	55	26	10.45	8.1e-22 (1.7e-20)

GO Biological Process, Cellular Component and Molecular Function categories independently corroborated this signature, surfacing: cellular response to interleukin-7 and type-II interferon, the MHC class I and II antigen-presentation machinery, and the cellular redox axis (cell redox homeostasis, response to oxidative stress, thioredoxin peroxidase activity) (Fig. 2C).

In an unbiased disease-annotation enrichment using the AGR ontology, bronchopulmonary dysplasia was significantly recovered as an enriched term in the full-list cargo signature (FE 3.67, p = 2.4 x 10^{-3}, BH-FDR 6.8 x 10^{-3}), alongside autoimmune disease, T-Cell acute lymphoblastic leukaemia, pulmonary fibrosis and a broader panel of chronic-inflammatory and pulmonary conditions (Fig. 2D and Table 2).

Table 2
Disease annotation AGR enrichments from PANGEA v2 analysis of the full MRG1061 proteomic cargo (n = 1,136). *Bronchopulmonary dysplasia* itself is significantly enriched (BH-FDR 0.007), alongside autoimmune disease and T-cell acute lymphoblastic leukaemia (BH-FDR < 0.05) and a broader chronic-inflammatory and pulmonary disease panel. Asterisks mark BH-FDR < 0.05.

Disease annotation	DOID	Set size	Overlap n	FE	P value (BH-FDR)
Bronchopulmonary dysplasia	DOID:9637	27	7	3.67	2.4e-03 (6.8e-03) *
Autoimmune disease	DOID:417	31	4	4.61	9.1e-03 (2.0e-02) *
T-cell acute lymphoblastic leukaemia	DOID:5603	35	4	4.07	1.4e-02 (3.0e-02) *
Pulmonary fibrosis	DOID:3770	165	10	1.99	2.8e-02 (5.3e-02)
Rheumatic heart disease	DOID:2298	43	4	3.29	3.0e-02 (5.5e-02)
Acute necrotising pancreatitis	DOID:0050700	72	5	2.54	4.4e-02 (7.6e-02)
Pulmonary emphysema	DOID:9675	38	5	1.96	1.1e-01 (1.6e-01)
Psoriasis	DOID:8893	52	8	1.65	1.1e-01 (1.7e-01)
Inflammatory bowel disease	DOID:0050589	119	6	1.79	1.2e-01 (1.7e-01)
Rheumatoid arthritis	DOID:7148	284	11	1.38	1.8e-01 (2.4e-01)
Pulmonary hypertension	DOID:6432	369	12	1.16	3.4e-01 (4.2e-01)
Chronic obstructive pulmonary disease	DOID:3083	337	10	1.06	4.7e-01 (5.5e-01)

Focusing on the 20 most abundant cargo proteins identified a coherent inflammation programme anchored by an actin-cytoskeleton / vesicle-release axis (Fig. 2E). Platelet degranulation was the standout Top-20 hit (FE 47, BH-FDR 9.9 x 10^{-6}), drive by ANXA5, CFL1, PFN1, TAGLN2 and RMSB4X. Negative regulation of stress-activated MAPK cascade (FE 218, BH-FDR 1.4 x 10^{-3}), Intrinsic Pathway for

Apoptosis (FE 89, BH-FDR 4.5 x 10^{-3}), MHC class II protein-complex binding (FE 73, BH-FDR 5.9 x 10^{-3}), Innate Immune System, Neutrophil degranulation, cellular response to type-II interferon, Cytokine Signalling in Immune System and regulation of canonical NF-κB signalling were all enriched. HSPA8 (six pathways), CFL1 (five) and GSTP1 (four) emerged as the dominant pathway-anchoring proteins (Fig. 2E). Full per-term statistics and gene-overlap lists for both the full and Top-20 analyses are provided in **Supplementary Table S2**.

Evaluation of anti-inflammatory proteomic predictions

To assess the ability of MRG1061 to modify pathways identified in the pathway enrichment analyses, we employed different human cell assays to measure effects at the gene and protein level. We first isolated and stimulated human peripheral blood mononuclear cells (PBMCs) with lipopolysaccharide (LPS), a known pro-inflammatory stimulus (42). LPS stimulation induced a significant increase in all inflammatory genes, including *TNF* (4.0 ± 0.6 to 25.4 ± 10.3), *IL6* (21.6 ± 24.7 to 863 ± 355), *NFKB1* (3.3 ± 2.0 to 12.4 ± 4.6), *IL1B* (24.5 ± 6.5 to 166 ± 60), and *CASP1* (2.6 ± 2.3 to 4.2 ± 2.0). The addition of MRG1061 significantly reduced the pro-inflammatory gene expression of *TNFα* and *IL6* (to 14.2 ± 1.9 and 431 ± 99.8 respectively) but had no effect on total *NF-κB* expression (9.3 ± 2.7) (Fig. 3A). Assessing NF-κB activity demonstrated a significant reduction in NF-κB protein activity in an adenocarcinomic human alveolar basal epithelial reporter cell line co-stimulated with MRG1061 and TNFα (from 360 ± 275 to 70.8 ± 33.4) or IL-1β (from 268 ± 94.9 to 69.3 ± 30.5) (Fig. 3B). To verify MRG1061's anti-inflammatory properties on a protein level, we then assessed TNFα concentration in PBMCs stimulated with LPS and treated with or without MRG1061. Concordant to the gene expression profile, MRG1061 reduced TNFα protein levels in a dose-dependant correlation by up to 59.0% (627 pg/mL ± 112 to a low of 282 pg/mL ± 58.2 between stimulated control and 10% v/v) (Fig. 3C).

To assess MRG1061's ability to regenerate human epithelial and mesenchymal lung cells, we used human primary alveolar epithelial cells and human lung fibroblasts and assessed their proliferation and senescence. When human primary alveolar epithelial cells were incubated with NSC23766 and MRG1061, their proliferation rate was significantly reduced compared to epithelial cells that were treated with NSC23766 alone (from 49.6% ± 10.8 to 39.7% ± 6.7) (Fig. 3D). Moreover, human lung fibroblasts stimulated with Etoposide showed increased β-galactosidase staining indicative of cellular senescence (13.7% ± 3.5 to 68.5% ± 7.5). Interestingly, MRG1061 reduced the level of stress-induced cellular senescence by 54.7% (to 31.0% ± 3.9) (Fig. 3E).

MRG1061 has regenerative and anti-inflammatory properties in an experimental BPD mouse model

We next assessed the ability of MRG1061 to modulate experimental BPD, a key enriched disease annotation in the proteomic analysis, in a neonatal hyperoxia mouse model (Fig. 4A). Overall survival throughout the experimental timeline did not differ among all groups, regardless of hyperoxia exposure or MRG1061 treatment, with 2 untreated control mice dying on day 1 and a single hyperoxia control

mouse dying at day 4 (Fig. 4B). Hyperoxia exposure and intraperitoneal saline treatment only at postnatal day 4, 6, and 8 decreased the number of alveoli in the lungs of neonatal mouse pups compared to control neonates from 3.61 ± 1.14 to 2.95 ± 1.1 (18.3% decrease). However, when hyperoxia-exposed neonatal mouse pups were treated intraperitoneally at postnatal day 4, 6, and 8 with MRG1061, alveolarisation was significantly improved back to 3.16 ± 1.21 (7.1% increase) (Fig. 4C). As inflammation is a hallmark of experimental and human BPD pathophysiology, we next assessed MRG1061 anti-inflammatory potential. Hyperoxia exposure and treatment with saline led to increased gene expression of pro-inflammatory cyto- and chemokines, including *TNF* and *CCL2* compared to controls (1.13 ± 0.6 to 1.91 ± 0.27 (69.0% increase) and 1.03 ± 0.26 to 6.62 ± 1.2 (542% increase) respectively). When treated with MRG1061, the gene expression of *TNF* and *CCL2* was significantly downregulated compared to hyperoxia-exposed neonatal mouse pups treated with saline only (to 1.2 ± 0.4 (37.2% decrease) and 4.08 ± 1.55 (38.4% decrease) respectively). Moreover, the gene expression of *CASP1* and *IL18*, which are part of the NLRP3 inflammasome cascade, was significantly reduced in hyperoxia-exposed/MRG1061-treated neonatal mouse lungs compared to hyperoxia-exposed and saline-treated neonates (from 1.27 ± 0.17 to 0.70 ± 0.08 (44.9% decrease) and 1.35 ± 0.27 to 0.85 ± 0.24 (37.0% decrease) respectively) (Fig. 4D).

Safety and distribution of MRG1061 in vivo

To investigate the ability of MRG1061 to interact with lung tissue, we investigated the uptake of EV-labelled MRG1061 in a human lung adenocarcinoma cell line. A549 cells showed a significant uptake of PKH-labelled MRG1061 that increased over time (Fig. 5A). We next assessed the potential safety profile of MRG1061 *in vivo* by monitoring blood serum biomarkers following intravenous (IV) administration of MRG1061 into healthy male and female mice on days 1, 7 and 28 (Fig. 5B). The presence of MRG1061 exerted no change to serum electrolytes (sodium, potassium, chloride, magnesium, calcium, inorganic phosphorus, iron), kidney function (urea, creatine), liver function (ALT, AST, total protein, albumin) and cholestasis parameters (total bilirubin, ALP), tissue injury enzymes (creatine kinase, lactate dehydrogenase), and metabolic markers (uric acid) regardless of the sex (Fig. 5C).

Discussion

In this study, we demonstrated that a stem cell-free therapeutic candidate (MRG1061) created using a proprietary platform, Secretomix®, has regenerative potential in an experimental mouse model of BPD, linked to a multi-modal action but primarily through anti-inflammatory pathways. Scientific interest in the therapeutic potential of stem cell paracrine factors lies in their multifaceted composition. As shown in the current study, MRG1061, derived from a GMP-validated amniotic fluid stem cell line, contains a wide variety of proteins and extracellular vesicles that orchestrate a diverse number of biological pathways, including attenuating inflammation. Inflammatory signalling cascades are key aspects in human and experimental BPD pathophysiology, leading to microvascular injury and blunted alveolarisation (1, 6, 43).

However, the pathogenesis of BPD is complex and inflammatory cascades are redundant. The development of BPD depends on the presence of certain risk factors, including chorioamnionitis, maternal smoking during pregnancy, or the occurrence of oligohydramnios due to preterm premature rupture of the membranes. Although numerous anti-inflammatory agents have shown promise in preclinical models of BPD, the additional risk factors and contributors to BPD pathophysiology may explain the unsuccessful clinical translation (44). Moreover, the degree of lung injury in BPD is inherently heterogeneous as some ELGAN developing BPD are born during the 22nd week of gestation (canalicular stage of lung development), whereas other ELGANs born during the 28th week of gestation also developing BPD have more mature lungs (saccular stage) (45). This positions stem cells and their derivatives with a heterogeneous bioactive cargo, such as MRG1061, as promising therapeutics to target a heterogeneous disease.

Preclinical evidence exists for the use of MSCs to treat or prevent experimental BPD and this is beginning to be translated into clinical trials, though to date, this work remains at the whole cell level rather than the paracrine factors from such cells (2, 15, 18, 46, 47). Intratracheal and IV routes of delivery have both demonstrated efficacy in experimental BPD with the mechanism of action suggested to be due to paracrine signalling and the release of bioactive molecules, as conditioned medium showed similar effects to the effects of their parent cells and low engraftment of the applied stem cells (18, 46). These findings were later followed up using a specific fraction of the conditioned medium: EVs, lipid-bound particles that are released by cells that carry a variety of bioactive molecules and play essential roles in communication and signalling between cells (27, 34, 35). MSC-EVs showed similar properties in small and large animal models of BPD with anti-inflammatory, regenerative and pro-angiogenic properties (19, 21, 22). AFSC-EVs have been more widely explored in the context of pulmonary hypoplasia secondary to congenital diaphragmatic hernia, where antenatal application of those EVs led to rescued lung development via immunomodulation of foetal lung macrophages, further highlighting the anti-inflammatory properties of amniotic fluid and multipotent stromal cells and their derivatives (20, 24, 28, 30, 36, 46).

Although the administration of MSCs and AFSCs was shown to be safe in immunocompetent and immunocompromised mouse/rat models (23), a cell-free approach using the secretome of the stem cells would be advantageous. First, as the therapeutic effects of stem cells are mainly exerted via paracrine signalling, the beneficial factors within the stem cell secretome can be enriched and may outperform the regenerative properties of their parent cells. Secondly, pharmaceutical production of large stem cell populations in a GMP-grade fashion would be expensive and less efficient than isolating stem cell secretome, especially if utilised as a conditioned media rather than further processing for any one component (27). Finally, although MSCs have demonstrated immunological safety when introduced whole, whole cell transplantation still represents risk, in the form of possible pulmonary embolism from aggregated cells or potential neoplasia if there are genetic alterations during *ex vivo* expansion (23, 48). In the current article, we were able to confirm that a secretome product, MRG1061 derived from a GMP-grade AFSC had regenerative and anti-inflammatory properties when administered intraperitoneally (IP)

in a mouse model of BPD; thus, confirming the anti-inflammatory effect of AFSCs via paracrine signalling.

Towards clinical translation, we also used various human cell lines and confirmed the anti-inflammatory and regenerative properties of MRG1061 on PBMCs, human primary alveolar epithelial cells, and human lung fibroblasts. We observed a dose-dependent reduction in TNFα concentration when LPS-stimulated PBMCs were treated with MRG1061, providing data towards clinically relevant immune-modulatory effects. Human primary alveolar epithelial cells were co-cultured with NSC23766, an inhibitor of RAC1 that is a Rho GTPase involved in regulating branching morphogenesis, mimicking disturbed epithelial development that would be observed in an ELGAN, a patient population most susceptible for the development of BPD (45, 49). Interestingly, administration of MRG1061 modulated the aberrant proliferation of human primary alveolar epithelial cells injured with NSC23766. This finding may be attributed to their regenerative capabilities and is in line with a previous study showing decreased proliferation of hepatic stellate cells when treated with adipose tissue-derived MSCs (50). Cellular senescence refers to a stable and irreversible halt in cell division that occurs in response to DNA-damaging stress and has been linked to BPD progression through elevated oxidative stress, inflammation and endoplasmic reticulum stress (51, 52). When human lung fibroblasts were treated with MRG1061, cellular senescence was significantly reduced compared to untreated and injured human lung fibroblasts, providing evidence towards the multi-model effect of a stem cell secretome.

Before taking this stem cell-based therapeutic candidate into a clinical trial, several additional preclinical steps must be taken. Although we have assessed the serum of mice treated with MRG1061 for electrolyte imbalances, liver & kidney function, tissue injury enzymes, and metabolic markers, further defined safety and toxicology studies are necessary to establish the safety of MRG1061. Moreover, the utilised BPD model depends on hyperoxia exposure alone which mimics lung architectural changes like those observed in humans with BPD (1). However, BPD is multifactorial and secondary to prenatal factors (e.g., chorioamnionitis), barotrauma (intubation and ventilation), hyperoxia exposure, and prematurity, among other risk factors (1). Thus, additional testing of MRG1061 in different models of BPD, such as secondary to LPS exposure in combination with hyperoxia, may give additional insights into its regenerative properties (53). Secondly, future research will explore the timing and frequency of MRG1061 application. In the current study, neonatal mouse pups were injected intraperitoneally during the 10-day experimental setup. It is unknown whether single-dose or higher frequencies are necessary to prevent and/or improve experimental BPD. Other studies investigating MSC-EVs have injected the therapy either IV or intratracheally (21, 54). Thus, one could speculate that the direct intratracheal approach may be advantageous to increase the therapeutic concentration in the target organ, here being the lung. Besides the frequency, dosing studies using experimental models are necessary to determine the optimal dose of MRG1061. Long-term follow up of pups recovering from hyperoxia exposure has not been conducted to define pulmonary and neurocognitive long-term outcome, which determines long-term morbidity in human patients recovering from BDP (1). Most importantly, large animal studies must be conducted as they allow the measurement of more functional outcome parameters beyond structural airway changes.

Conclusion

The current study provides evidence for regenerative and anti-inflammatory properties of stem cell-free therapeutic MRG1061 treatment for experimental BPD. Before this promising therapy can be offered to patients in clinical reality, additional steps must be taken to determine potential off-target side-effects, pharmacodynamic and pharmacokinetic considerations for dosing and application frequency.

Abbreviations

AFSCs Amniotic fluid
derived stem cells

Declarations

Ethics approval and consent to participate:

Informed written consent was obtained from all human donors (or their legal representatives) prior to their participation in the study, including consent for the storage and use of tissue samples for research purposes. Studies were approved by the relevant ethics committee detailed below:

Consent for publication:

Not applicable

Competing Interests

RM, AP, KP, SR are employed by Micregen Ltd.

Funding:

The work was funded by Micregen Limited

Author Contribution

Conceptualisation: RM, KPWriting – Original draft: RM, FDWriting – Review and Editing: RM, FD, AZ, KP, AP, SR, DW, BMSupervision: RM, KP, AZ, DWInvestigation: LA, FD, DF, RLF, VF, KK, AA, EL, AR, KS, APRM and KP are joint-last authors

Acknowledgement

Biorender.com was used for graphical illustration. During the preparation of this manuscript, the authors used ChatGPT-5 to enhance the clarity and readability of portions of the manuscript and Claude to visualise the PANGEA bioinformatic output. All such sections were carefully reviewed and revised as necessary. The authors take full responsibility for the accuracy and integrity of the scientific content. We would like to thank the Imaging Facility, and the Lab Animal Services at the Peter Gilgan Center for Research and Learning at The Hospital for Sick Children (SickKids), Toronto. The authors would like to thank Dr's. Martin Post and Sheena Bouch for their help with the hyperoxia Plexiglas chamber handling and Prof. Joern Dengjel at Universität Freiburg for LC-MS/MS processing.

Data Availability

All data generated or analysed during this study are included in this publication and its supplementary information files.

References

1. Thebaud B, Goss KN, Laughon M, Whitsett JA, Abman SH, Steinhorn RH, et al. Bronchopulmonary dysplasia. Nat Rev Dis Primers. 2019;5(1):78.
2. Durlak W, Thebaud B. BPD: Latest Strategies of Prevention and Treatment. Neonatology. 2024;121(5):596–607.
3. Quach H, Farrell S, Wu MJM, Kanagarajah K, Leung JW, Xu X, et al. Early human fetal lung atlas reveals the temporal dynamics of epithelial cell plasticity. Nat Commun. 2024;15(1):5898.
4. Negretti NM, Plosa EJ, Benjamin JT, Schuler BA, Habermann AC, Jetter CS et al. A single-cell atlas of mouse lung development. Development. 2021;148(24).
5. Doktor F, Antounians L, Lacher M, Zani A. Congenital lung malformations: Dysregulated lung developmental processes and altered signaling pathways. Semin Pediatr Surg. 2022;31(6):151228.
6. Hurskainen M, Mizikova I, Cook DP, Andersson N, Cyr-Depauw C, Lesage F, et al. Single cell transcriptomic analysis of murine lung development on hyperoxia-induced damage. Nat Commun. 2021;12(1):1565.
7. Horbar JD, Edwards EM, Greenberg LT, Morrow KA, Soll RF, Buus-Frank ME, et al. Variation in Performance of Neonatal Intensive Care Units in the United States. JAMA Pediatr. 2017;171(3):e164396.
8. Schmidt B, Roberts RS, Davis P, Doyle LW, Barrington KJ, Ohlsson A, et al. Caffeine therapy for apnea of prematurity. N Engl J Med. 2006;354(20):2112–21.
9. Schmidt B, Roberts RS, Davis P, Doyle LW, Barrington KJ, Ohlsson A, et al. Long-term effects of caffeine therapy for apnea of prematurity. N Engl J Med. 2007;357(19):1893–902.
10. Askie LM, Darlow BA, Finer N, Schmidt B, Stenson B, Tarnow-Mordi W, et al. Association Between Oxygen Saturation Targeting and Death or Disability in Extremely Preterm Infants in the Neonatal

Oxygenation Prospective Meta-analysis Collaboration. JAMA. 2018;319(21):2190–201.

11. Cools F, Offringa M, Askie LM. Elective high frequency oscillatory ventilation versus conventional ventilation for acute pulmonary dysfunction in preterm infants. Cochrane Database Syst Rev. 2015;2015(3):CD000104.
12. Klingenberg C, Wheeler KI, McCallion N, Morley CJ, Davis PG. Volume-targeted versus pressure-limited ventilation in neonates. Cochrane Database Syst Rev. 2017;10(10):CD003666.
13. Doyle LW, Cheong JL, Hay S, Manley BJ, Halliday HL. Late (>/= 7 days) systemic postnatal corticosteroids for prevention of bronchopulmonary dysplasia in preterm infants. Cochrane Database Syst Rev. 2021;11(11):CD001145.
14. Doyle LW, Cheong JL, Hay S, Manley BJ, Halliday HL. Early (< 7 days) systemic postnatal corticosteroids for prevention of bronchopulmonary dysplasia in preterm infants. Cochrane Database Syst Rev. 2021;10(10):CD001146.
15. Augustine S, Cheng W, Avey MT, Chan ML, Lingappa SMC, Hutton B, et al. Are all stem cells equal? Systematic review, evidence map, and meta-analyses of preclinical stem cell-based therapies for bronchopulmonary dysplasia. Stem Cells Transl Med. 2020;9(2):158–68.
16. Zani A, Cananzi M, Fascetti-Leon F, Lauriti G, Smith VV, Bollini S, et al. Amniotic fluid stem cells improve survival and enhance repair of damaged intestine in necrotising enterocolitis via a COX-2 dependent mechanism. Gut. 2014;63(2):300–9.
17. Pederiva F, Ghionzoli M, Pierro A, De Coppi P, Tovar JA. Amniotic fluid stem cells rescue both in vitro and in vivo growth, innervation, and motility in nitrofen-exposed hypoplastic rat lungs through paracrine effects. Cell Transpl. 2013;22(9):1683–94.
18. Pierro M, Ionescu L, Montemurro T, Vadivel A, Weissmann G, Oudit G, et al. Short-term, long-term and paracrine effect of human umbilical cord-derived stem cells in lung injury prevention and repair in experimental bronchopulmonary dysplasia. Thorax. 2013;68(5):475–84.
19. Albertine KH, Rebentisch A, Dawson E, Van Boerum J, Major E, Stipka J, et al. Mesenchymal stromal cell extracellular vesicles improve lung development in mechanically ventilated preterm lambs. Am J Physiol Lung Cell Mol Physiol. 2024;326(6):L770–85.
20. Willis GR, Fernandez-Gonzalez A, Anastas J, Vitali SH, Liu X, Ericsson M, et al. Mesenchymal Stromal Cell Exosomes Ameliorate Experimental Bronchopulmonary Dysplasia and Restore Lung Function through Macrophage Immunomodulation. Am J Respir Crit Care Med. 2018;197(1):104–16.
21. Willis GR, Fernandez-Gonzalez A, Reis M, Yeung V, Liu X, Ericsson M, et al. Mesenchymal stromal cell-derived small extracellular vesicles restore lung architecture and improve exercise capacity in a model of neonatal hyperoxia-induced lung injury. J Extracell Vesicles. 2020;9(1):1790874.
22. Willis GR, Reis M, Gheinani AH, Fernandez-Gonzalez A, Taglauer ES, Yeung V, et al. Extracellular Vesicles Protect the Neonatal Lung from Hyperoxic Injury through the Epigenetic and Transcriptomic Reprogramming of Myeloid Cells. Am J Respir Crit Care Med. 2021;204(12):1418–32.
23. De Coppi P, Bartsch G Jr., Siddiqui MM, Xu T, Santos CC, Perin L, et al. Isolation of amniotic stem cell lines with potential for therapy. Nat Biotechnol. 2007;25(1):100–6.

24. Loukogeorgakis SP, De Coppi P, Concise Review. Amniotic Fluid Stem Cells: The Known, the Unknown, and Potential Regenerative Medicine Applications. Stem Cells. 2017;35(7):1663–73.
25. Garcia O, Carraro G, Turcatel G, Hall M, Sedrakyan S, Roche T, et al. Amniotic fluid stem cells inhibit the progression of bleomycin-induced pulmonary fibrosis via CCL2 modulation in bronchoalveolar lavage. PLoS ONE. 2013;8(8):e71679.
26. Doktor F, Figueira RL, Fortuna V, Biouss G, Stasiewicz K, Obed M, et al. Amniotic fluid stem cell extracellular vesicles promote lung development via TGF-beta modulation in a fetal rat model of oligohydramnios. J Control Release. 2025;377:427–41.
27. Doktor F, Antounians L, Figueira RL, Khalaj K, Duci M, Zani A. Amniotic fluid stem cell extracellular vesicles as a novel fetal therapy for pulmonary hypoplasia: a review on mechanisms and translational potential. Stem Cells Transl Med. 2025;14(1).
28. Antounians L, Figueira RL, Kukreja B, Litvack ML, Zani-Ruttenstock E, Khalaj K, et al. Fetal hypoplastic lungs have multilineage inflammation that is reversed by amniotic fluid stem cell extracellular vesicle treatment. Sci Adv. 2024;10(30):eadn5405.
29. Doktor F, Lo E, Fortuna V, Khalaj K, Garcia M, Figueira RL, et al. Sex-specific differences in the severity of pulmonary hypoplasia in experimental congenital diaphragmatic hernia and implications for extracellular vesicle-based therapy. Pediatr Surg Int. 2024;40(1):278.
30. Figueira RL, Khoshgoo N, Doktor F, Khalaj K, Islam T, Moheimani N, et al. Antenatal Administration of Extracellular Vesicles Derived From Amniotic Fluid Stem Cells Improves Lung Function in Neonatal Rats With Congenital Diaphragmatic Hernia. J Pediatr Surg. 2024;59(9):1771–7.
31. Antounians L, Catania VD, Montalva L, Liu BD, Hou H, Chan C, et al. Fetal lung underdevelopment is rescued by administration of amniotic fluid stem cell extracellular vesicles in rodents. Sci Transl Med. 2021;13:590.
32. Khalaj K, Figueira RL, Antounians L, Gandhi S, Wales M, Montalva L, et al. Treatment with Amniotic Fluid Stem Cell Extracellular Vesicles Promotes Fetal Lung Branching and Cell Differentiation at Canalicular and Saccular Stages in Experimental Pulmonary Hypoplasia Secondary to Congenital Diaphragmatic Hernia. Stem Cells Transl Med. 2022;11(10):1089–102.
33. Khalaj K, Antounians L, Figueira RL, Post M, Zani A. Autophagy Is Impaired in Fetal Hypoplastic Lungs and Rescued by Administration of Amniotic Fluid Stem Cell Extracellular Vesicles. Am J Respir Crit Care Med. 2022;206(4):476–87.
34. Mitchell R, Mellows B, Sheard J, Antonioli M, Kretz O, Chambers D, et al. Secretome of adipose-derived mesenchymal stem cells promotes skeletal muscle regeneration through synergistic action of extracellular vesicle cargo and soluble proteins. Stem Cell Res Ther. 2019;10(1):116.
35. Mellows B, Mitchell R, Antonioli M, Kretz O, Chambers D, Zeuner MT, et al. Protein and Molecular Characterization of a Clinically Compliant Amniotic Fluid Stem Cell-Derived Extracellular Vesicle Fraction Capable of Accelerating Muscle Regeneration Through Enhancement of Angiogenesis. Stem Cells Dev. 2017;26(18):1316–33.

36. Blundell M, Doktor F, Figueira RL, Khalaj K, Biouss G, Antounians L, et al. Anti-inflammatory effects of antenatal administration of stem cell derived extracellular vesicles in the brain of rat fetuses with congenital diaphragmatic hernia. Pediatr Surg Int. 2023;39(1):291.
37. Bustin SA, Benes V, Garson JA, Hellemans J, Huggett J, Kubista M, et al. The MIQE guidelines: minimum information for publication of quantitative real-time PCR experiments. Clin Chem. 2009;55(4):611–22.
38. Zeuner MT, Vallance T, Vaiyapuri S, Cottrell GS, Widera D. Development and Characterisation of a Novel NF-kappaB Reporter Cell Line for Investigation of Neuroinflammation. Mediators Inflamm. 2017;2017:6209865.
39. Nardiello C, Mizikova I, Silva DM, Ruiz-Camp J, Mayer K, Vadasz I, et al. Standardisation of oxygen exposure in the development of mouse models for bronchopulmonary dysplasia. Dis Model Mech. 2017;10(2):185–96.
40. Feddersen S, Nardiello C, Selvakumar B, Vadasz I, Herold S, Seeger W, et al. Impact of litter size on survival, growth and lung alveolarization of newborn mouse pups. Ann Anat. 2020;232:151579.
41. Dominici M, Le Blanc K, Mueller I, Slaper-Cortenbach I, Marini F, Krause D, et al. Minimal criteria for defining multipotent mesenchymal stromal cells. The International Society for Cellular Therapy position statement. Cytotherapy. 2006;8(4):315–7.
42. Ngkelo A, Meja K, Yeadon M, Adcock I, Kirkham PA. LPS induced inflammatory responses in human peripheral blood mononuclear cells is mediated through NOX4 and Gialpha dependent PI-3kinase signalling. J Inflamm (Lond). 2012;9(1):1.
43. Liao J, Kapadia VS, Brown LS, Cheong N, Longoria C, Mija D, et al. The NLRP3 inflammasome is critically involved in the development of bronchopulmonary dysplasia. Nat Commun. 2015;6:8977.
44. Surate Solaligue DE, Rodriguez-Castillo JA, Ahlbrecht K, Morty RE. Recent advances in our understanding of the mechanisms of late lung development and bronchopulmonary dysplasia. Am J Physiol Lung Cell Mol Physiol. 2017;313(6):L1101–53.
45. Deguise MO, Thebaud B. The Role of Mesenchymal Stromal Cells in the Treatment of Bronchopulmonary Dysplasia: A Multi-Prong Approach for a Heterogeneous Disease. Compr Physiol. 2025;15(4):e70038.
46. Aslam M, Baveja R, Liang OD, Fernandez-Gonzalez A, Lee C, Mitsialis SA, et al. Bone marrow stromal cells attenuate lung injury in a murine model of neonatal chronic lung disease. Am J Respir Crit Care Med. 2009;180(11):1122–30.
47. Grisafi D, Pozzobon M, Dedja A, Vanzo V, Tomanin R, Porzionato A, et al. Human amniotic fluid stem cells protect rat lungs exposed to moderate hyperoxia. Pediatr Pulmonol. 2013;48(11):1070–80.
48. Cohen JA. Mesenchymal stem cell transplantation in multiple sclerosis. J Neurol Sci. 2013;333(1–2):43–9.
49. Danopoulos S, Krainock M, Toubat O, Thornton M, Grubbs B, Al Alam D. Rac1 modulates mammalian lung branching morphogenesis in part through canonical Wnt signaling. Am J Physiol Lung Cell Mol Physiol. 2016;311(6):L1036–49.

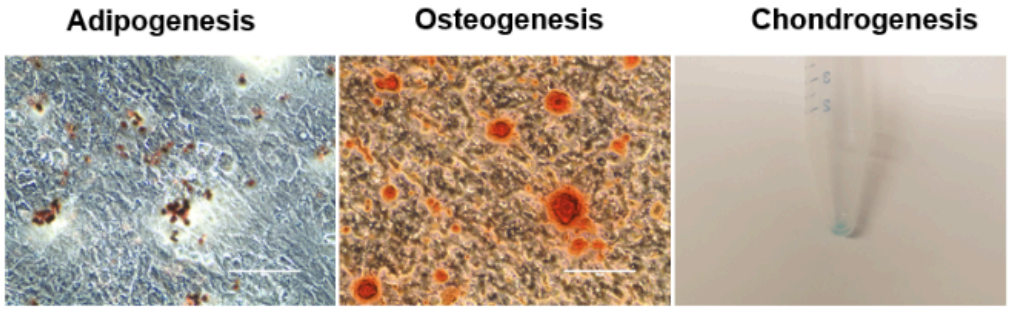
50. Lou G, Yang Y, Liu F, Ye B, Chen Z, Zheng M, et al. MiR-122 modification enhances the therapeutic efficacy of adipose tissue-derived mesenchymal stem cells against liver fibrosis. J Cell Mol Med. 2017;21(11):2963–73.
51. Koloko Ngassie ML, Drake LY, Roos BB, Koenig-Kappes A, Pabelick CM, Gosens R, et al. Endoplasmic reticulum stress-induced senescence in human lung fibroblasts. Am J Physiol Lung Cell Mol Physiol. 2024;327(1):L126–39.
52. Jing X, Jia S, Teng M, Day BW, Afolayan AJ, Jarzembowski JA, et al. Cellular Senescence Contributes to the Progression of Hyperoxic Bronchopulmonary Dysplasia. Am J Respir Cell Mol Biol. 2024;70(2):94–109.
53. Cyr-Depauw C, Hurskainen M, Vadivel A, Mizikova I, Lesage F, Thebaud B. Characterization of the innate immune response in a novel murine model mimicking bronchopulmonary dysplasia. Pediatr Res. 2021;89(4):803–13.
54. Lithopoulos MA, Strueby L, O'Reilly M, Zhong S, Mobius MA, Eaton F, et al. Pulmonary and Neurologic Effects of Mesenchymal Stromal Cell Extracellular Vesicles in a Multifactorial Lung Injury Model. Am J Respir Crit Care Med. 2022;205(10):1186–201.
55. Nichols WW, Murphy DG, Cristofalo VJ, Toji LH, Greene AE, Dwight SA. Characterization of a new human diploid cell strain, IMR-90. Science. 1977;196(4285):60–3.

Figures

Figure 1

A)

CD73	CD90	CD105	CD14	CD19	CD34	CD45	HLA-DR
99.60 ± 0.04	99.40 ± 0.20	99.65 ± 0.05	0.55 ± 0.10	0.50 ± 0.11	1.03 ± 0.11	0.70 ± 0.18	0.85 ± 0.23



B)

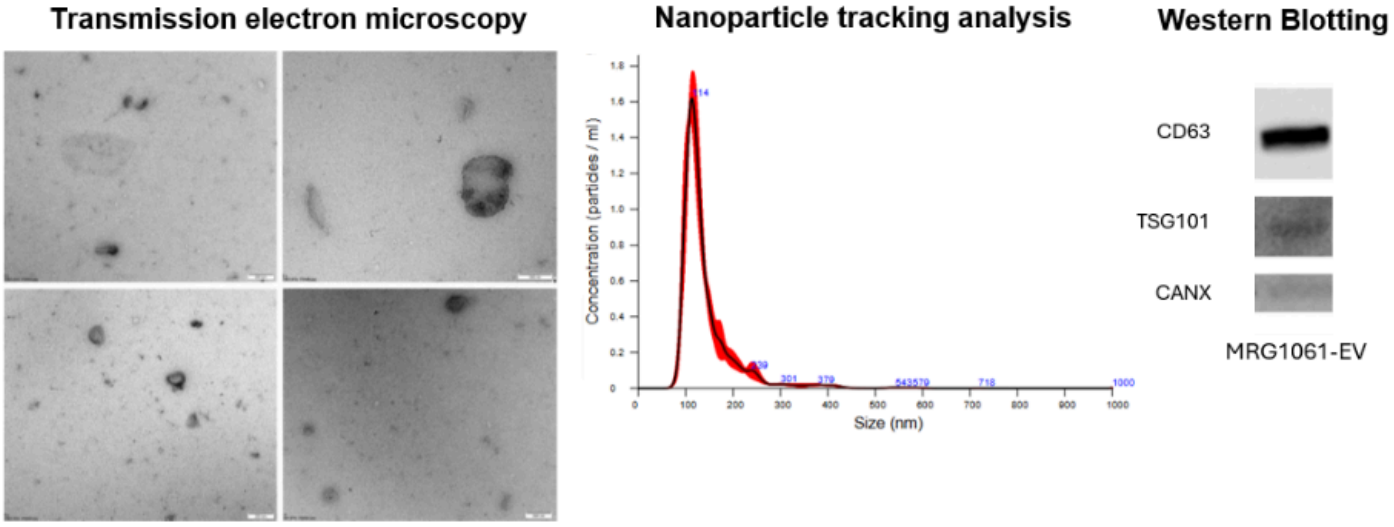


Figure 1

Characterisation of amniotic fluid-derived multipotent stromal cell and their extracellular vesicle content. **A)** MSC marker expression profile and tri-lineage profile of the AFSC population. **B)**TEM visualisation of EV morphology (left panel), size range of EV's assessed via NTA analysis (middle panel), and expression of canonical EV markers (right panel).

Figure 2

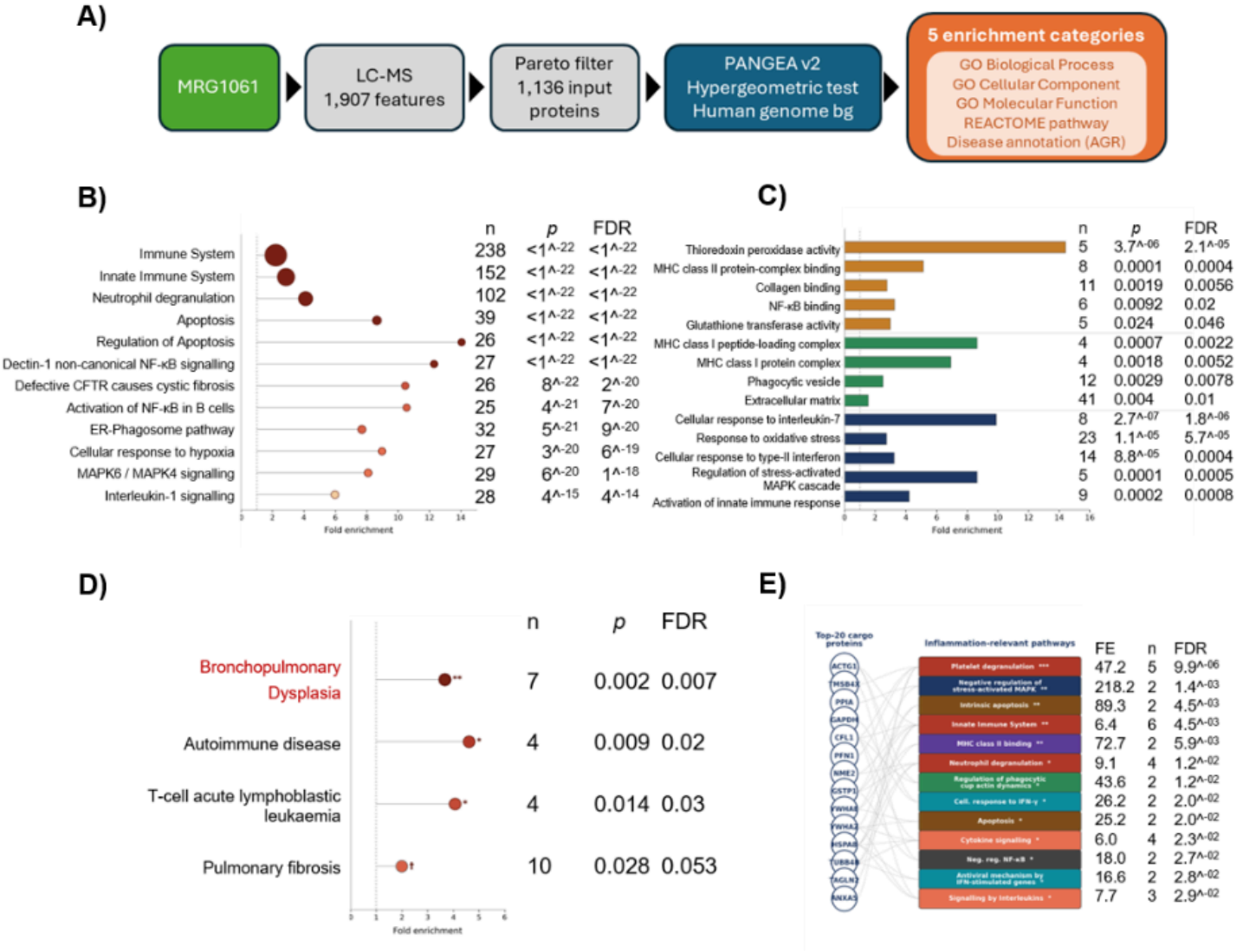


Figure 2

Proteomic-pathway analysis of the MRG1061 cargo identifies a coherent inflammation-modulating signature with unbiased recovery of bronchopulmonary dysplasia. **A)** Analysis workflow. The MRG1061 secretome was analysed by LC-MS proteomics; 1,907 features were quantified, of which 1,136 (positive Pareto scaling) defined the analysis input. Pathway enrichment was performed in PANGEA v2 using a hypergeometric test against the human genome background, with Bonferroni, Benjamini–Hochberg and Benjamini–Yekutieli correction, across Direct GO Biological Process, Cellular Component, Molecular Function, REACTOME pathway and Disease annotation (AGR) categories. **B)** Top inflammation-relevant REACTOME pathways. Dot plot of pathways spanning innate immunity / neutrophil biology, NF-κB signalling, apoptosis / programmed cell death, phagocytosis, the hypoxia response, MAPK signalling and the fibrosis / CFTR axis; sorted by Benjamini–Hochberg FDR. Dot size ∝ overlap count, colour ∝ $-\log_{10}$(BH-FDR). **C)** Category-stratified inflammation hits. Top inflammation-relevant terms by Direct GO Biological Process, Cellular Component and Molecular Function. **D)** Disease annotation enrichments.

Bronchopulmonary dysplasia is recovered as a significantly enriched disease annotation (asterisk: BH-FDR < 0.05), alongside pulmonary fibrosis and a broader inflammatory / autoimmune panel. **E)** Top 20 protein–pathway network. The 20 most-abundant cargo proteins and the inflammation-relevant pathways they participate in. Node size for proteins ∝ abundance rank; for pathways ∝ $-\log_{10}$ P value; edges encode pathway membership. Protein nodes contributing to the NLRP3 inflammasome and VEGFA–VEGFR2 pathways are marked.

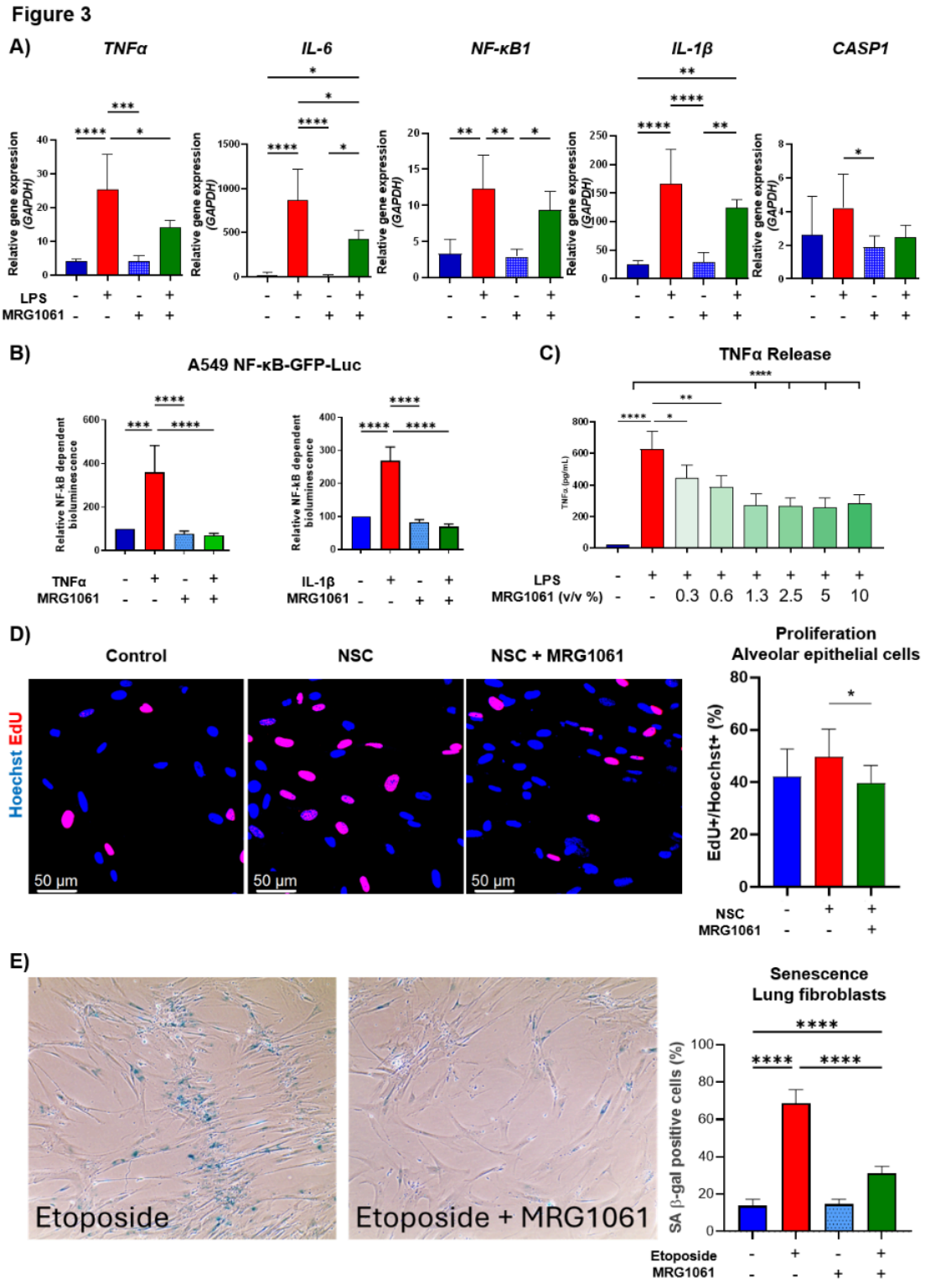


Figure 3

MRG1061 has anti-inflammatory and regenerative effects in human PBMCs, lung epithelial, and lung mesenchymal cell lineages. **A)** Gene expression changes were assessed via RT-qPCR for *TNFα*, *IL6*, *NFKB1*, *IL1B*, and *CASP1* between untreated PBMCs (blue), LPS-stimulated PBCMs (red), unstimulated but MRG1061-treated PBMCs (blue hatching), and LPS stimulated and MRG1061 treated PBMCs (green). Each group consists of at least n=5 biological replicates. **B)** Activity of NF-κB was robustly activated by either TNFα or IL-1β and reduced by co-administration of MRG1061. **C)** Dose response modulation of TNFα protein expression in untreated PBMCs (blue), LPS-stimulated PBCMs (red), and LPS-stimulated and MRG1061-treated PBMCs (green gradient). **D)**Proliferating cells from 3 experimental groups were compared and representative images are shown: Control (blue), cells injured with NSC23766 (red, NSC), and cells injured with NSC23766 and treated with MRG1061 (NSC+MRG1061). Proliferation was assessed by comparing EdU+ cells divided by all cells and is expressed as a percentage. **E)** Representative images for β-Galactosidase activity and ability of MRG1061 to modulate stress-induced cellular senescence comparing untreated human lung fibroblasts (IMR90 cells), Etoposide-stimulated human lung fibroblasts, unstimulated but MRG1061-treated human lung fibroblasts (blue hatching), and Etoposide-stimulated and MRG1061 treated human lung fibroblasts (green). Each group consists of at least n=5 biological replicates. $p<0.05$ was considered as statistically significant.

Figure 4

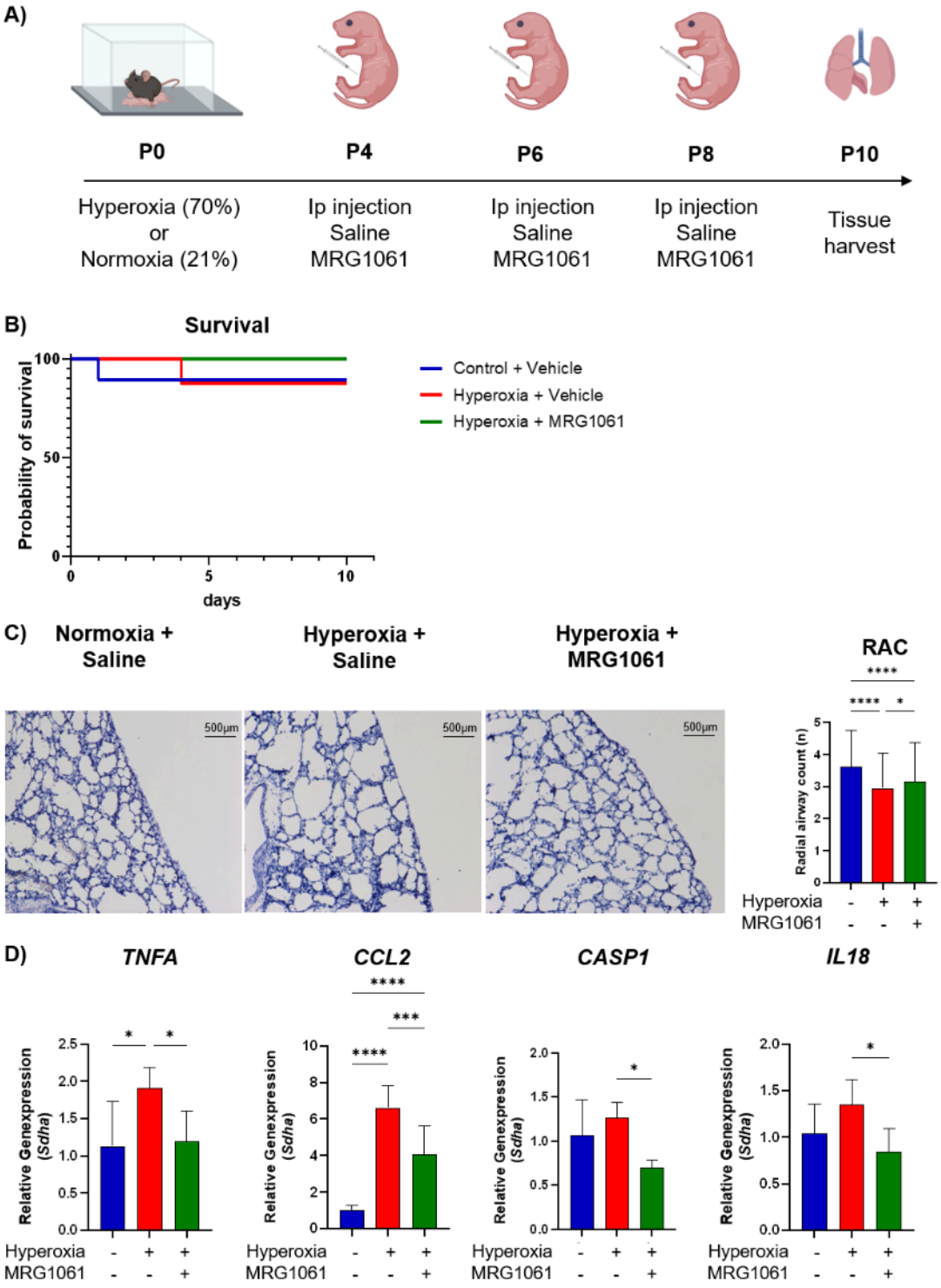


Figure 4

MRG1061 improves lung alveolarisation in an experimental BPD mouse model. **A)**Experimental timeline of hyperoxia exposure and MRG1061 application. **B)**Kaplan-Meier curve of survival over a time-course of 10 days comparing control pups (n=19, blue), hyperoxia-injured neonatal pups treated with saline only (n=8, red), or treated with MRG1061 (n=5, green). **C)** 3 representative images and analysis of the radial airway count (RAC) from the control (n= 4, blue), hyperoxia injured (n= 5, red), and hyperoxia injured-

MRG1061 treated group (n= 5, green). Technical replicates were used to determine statistical significance of 4 biological samples in the control group, and 5 biological samples in the hyperoxia+saline and hyperoxia+MRG1061 groups, respectively. **D)** Gene expression changes were assessed via RT-qPCR for *Tnf*, *ccl2*, *Casp1*, and *Il18* between normoxia exposed control pups (blue), hyperoxia exposed pups treated with saline only (red) or hyperoxia exposed pups treated with MRG1061 (green). Each group consists of at least n=4 biological replicates. $p<0.05$ was considered as statistically significant.

Figure 5

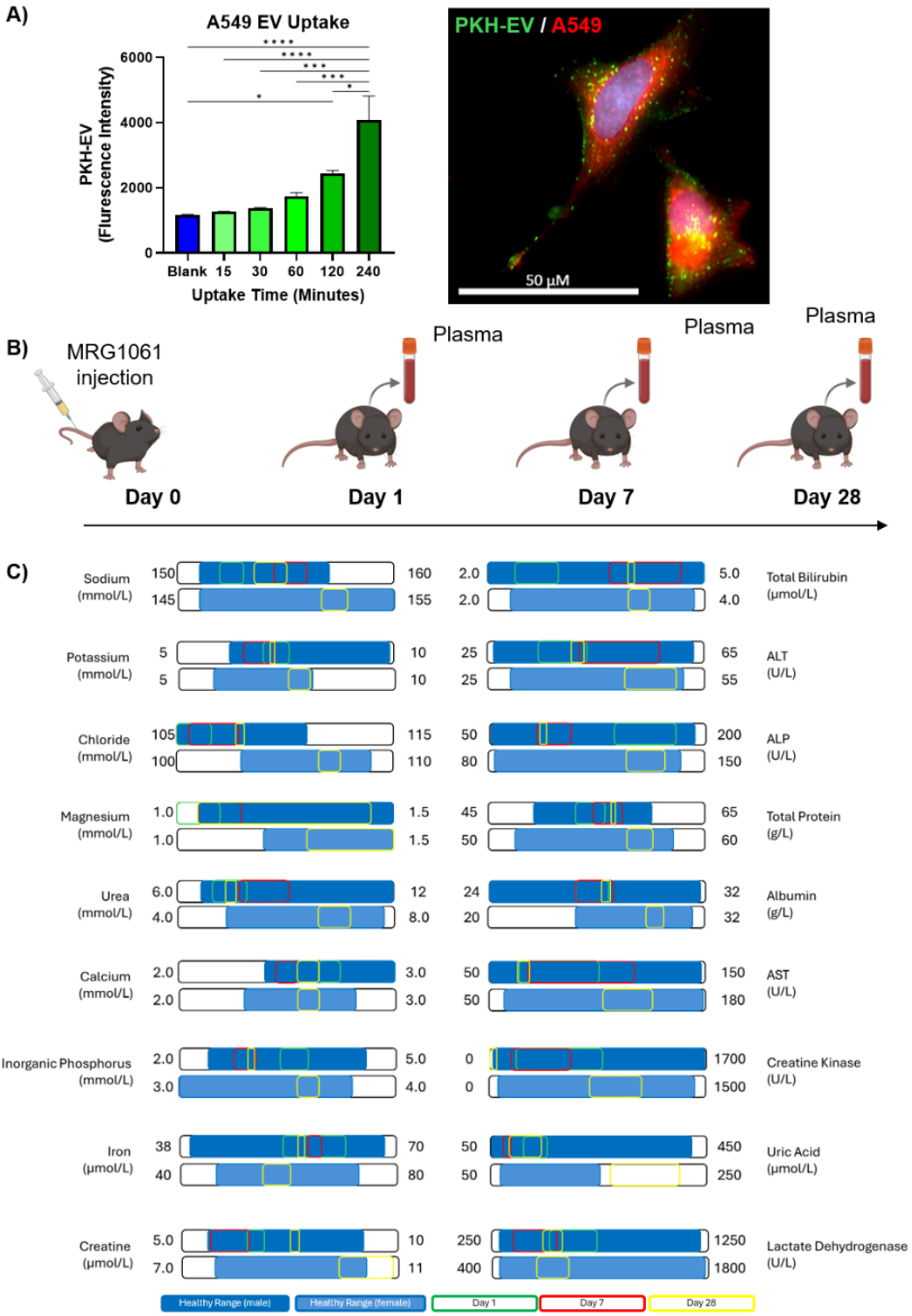


Figure 5

MRG1061 EV are taken up by lung cells *in vitro* and demonstrate little change in blood-borne safety biomarkers. **A)** Fluorescently labelled EV from MRG1061 are taken up by human lung cell A549 in a time-dependent manner. **B)** A schematic of *in vivo* 30 toxicological study. **C)** Common blood biomarkers are unchanged in male or female mice following repeat administration of MRG1061 over 28 days.

Supplementary Files

This is a list of supplementary files associated with this preprint. Click to download.

- SuppTableS1completePANGEAenrichment.xlsx
- SuppTableS2inflammationcuratedenrichment.xlsx
- SuppTableS3SequencelistofprimersusedforqPCRanalysis.xlsx
- SuppTableS4Antibodiesusedinthecurrentstudy.xlsx
- Doktoretal.SupplementaryFileUncroppedWesternBlot.pptx